

Crystallographic and electronic structures of three different polymorphs of pentacene

Hiroyuki Yoshida* and Naoki Sato

Institute for Chemical Research, Kyoto University, Uji, Kyoto 611-0011, Japan

(Received 7 September 2007; revised manuscript received 27 December 2007; published 10 June 2008)

Calculations are presented for the energy bands of three polymorphs of pentacene: the thin-film, bulk, and single-crystal phases. In the calculation of the thin-film phase, the structural data from our recent results on the x-ray diffraction reciprocal space mapping were applied. The band structures are essentially two dimensional, i.e., only small dispersions are found along the c^* direction. The energy dispersion of the thin-film phase is found to be larger and more isotropic than those of the other phases. The energy dispersions of the bands derived from highest occupied molecular orbital (HOMO), HOMO-1, lowest unoccupied molecular orbital (LUMO), and LUMO+1 levels are analyzed by comparing with the corresponding results on the basis of the tight-binding approximation; the dispersions are well described by transfer integrals involving only the nearest neighbor molecules. In accordance with this finding, a simple model is presented to explain the relation between the crystal structure and the energy dispersion. From the calculated bands, the effective masses are derived to discuss the transport properties of the hole and electrons. Angle-integrated photoemission spectra were also measured for the thin-film and bulk phases. Finally, spectral features of the HOMO-derived bands are interpreted by the calculated density of states.

DOI: [10.1103/PhysRevB.77.235205](https://doi.org/10.1103/PhysRevB.77.235205)

PACS number(s): 71.20.Rv, 72.80.Le, 79.60.Fr, 68.55.-a

I. INTRODUCTION

The electronic structure of organic semiconducting materials has received considerable attention from the viewpoint of both fundamental research and device applications. Since organic molecules form crystals owing to weak intermolecular interactions such as dispersion and electrostatic forces, the electronic structure in the solid states is primarily determined by that of the isolated molecule through those intramolecular interactions.¹ In this decade, however, the intermolecular energy bands have been experimentally observed in organic thin films of bis(1,2,5-thiadiazolo)-*p*-quinobis(1,3-dithiole) (BTQBT)^{2,3}, perylene-3,4,9,10-tetracarboxylic dianhydride (PTCDA)^{4,5}, discotic liquid crystals,⁶ and pentacene.⁷⁻⁹ The magnitude of the energy dispersions is a few 100 meV which indicates that the band transport of charge carriers is possible in organic solids. The temperature dependence of the charge carrier mobility at low temperature supports the band transport model.¹⁰

Among these molecular solids, energy band formation in pentacene attracts particularly our interests because pentacene is one of the most intensively studied materials as a working layer of an organic field-effect transistor; a field-effect mobility of $1 \text{ cm}^2 \text{ V}^{-1} \text{ s}^{-1}$ is often obtained in thin films, and $58 \times 10 \text{ cm}^2 \text{ V}^{-1} \text{ s}^{-1}$ is achieved in the single crystal.¹¹

Energy band calculations of pentacene have been carried out by several groups.¹²⁻²⁰ Since the energy band dispersion is imposed by the intermolecular interactions, the crystallographic structure used in the calculation is important. Several polymorphs are reported for pentacene crystals and thin films. The structure of the “single-crystal” phase ($d_{001} = 1.41 \text{ nm}$) (Refs. 21 and 22) has already been determined with x-ray analysis of the single crystal. The “bulk” phase ($d_{001} = 1.44 \text{ nm}$) was first found in thick vacuum-deposited films^{23,24} and organic solvent-treated films.²⁵ Although there were confusion about its structure, we have confirmed²⁶ that

the structure coincides with that of the single crystal reported by Campbell *et al.*²⁷ On the other hand, thin films fabricated on insulator surfaces such as silicon oxide (SiO_2) often show the “thin-film” phase characterized by $d_{001} = 1.54 \text{ nm}$. Since this phase is only found in films thinner than 100 nm, complete structural data was not obtained, despite various efforts using electron diffraction (ED)²⁸⁻³² or grazing incidence x-ray diffraction (GIXD).³³⁻³⁵ Even the identity of the crystal system among orthorhombic, monoclinic, and triclinic lattice types has not been determined as only the periodicity in the plane parallel to the substrate surface can be examined with these methods. As a result, most of the band calculations were made for the single-crystal^{12-15,17,18} and bulk¹⁵⁻²⁰ phases.

The band structure of the thin-film phase is, however, the most interesting because this phase is found in the pentacene thin films applied in the field-effect transistors. In fact, the band calculation for the thin-film phase has been attempted under the limited knowledge about its structural information:¹⁸⁻²⁰ Orthorhombic lattices were frequently assumed, and model structures were estimated from unreliable lattice parameters with the aid of molecular mechanics calculations.^{19,20} In the structure optimization, the potential energy surface of pentacene crystals has many local minima³⁶ that yield several different structures, so determining a most plausible structure is not a trivial task.

Recently, we have employed x-ray reciprocal space mapping (RSM) to determine the lattice parameters of the pentacene thin-film phase.³⁷ This method enabled us to measure structural periodicity along any direction including those neither parallel to nor normal to the substrate surface plane, in contrast to those only of surface plane in ED and GIXD and of surface normal in the θ - 2θ scan of x-ray diffraction. Diffraction data obtained by RSM are indispensable to determine the lattice parameters of low symmetric crystals such as monoclinic or triclinic. With the aid of RSM, we found that the thin-film phase had a triclinic lattice and the complete set of the lattice parameters was obtained.

TABLE I. Lattice parameters and molecular orientations for two inequivalent pentacene molecules (expressed by Euler angles) for the thin-film (Ref. 37), bulk (Refs. 27 and 41), and single-crystal (Ref. 22) phases. The lattice parameters of the bulk phase have been changed from the original ones to facilitate comparison with other polymorphs. The molecular orientations in the thin-film phase were optimized with two different force fields, Dreiding force field (a) and COMPASS (b), for the check of the effect from their difference.

Phase	Lattice parameter						Euler angle		
	a (nm)	b (nm)	c (nm)	α (deg)	β (deg)	γ (deg)	ω (deg)	χ (deg)	ϕ (deg)
Thin film ^a	0.593	0.756	1.565	98.6	93.3	89.8	215.4	176.7	150.2
							87.2	4.3	337.9
Thin film ^b	0.593	0.756	1.565	98.6	93.3	89.8	124.6	5.5	350.4
							77.6	6.5	346.9
Bulk	0.6079	0.7893	1.478	83.20	79.92	94.40	164.9	159.0	53.6
							64.9	22.5	231.3
Single crystal	0.6266	0.7775	1.4530	76.475	87.682	84.684	203.2	155.8	134.9
							109.3	24.6	313.9

In this work, we calculated the energy bands of the three polymorphs of pentacene, i.e., the thin-film, bulk, and single-crystal phases. A detailed analysis of the band structures was made in accordance with the tight-binding model. The effective masses and the densities of states (DOS) were then derived from the calculated band structure. Since the identity of the polymorphs was not considered explicitly in the previous ultraviolet photoemission spectroscopy (UPS) studies,^{38,39} angle-integrated ultraviolet photoemission spectra were also measured for the thin film and bulk phases. The spectral line shape of the highest occupied molecular orbital (HOMO)-derived feature in the UPS spectra was examined by comparing with the calculated DOS.

II. METHOD OF CALCULATION

The structure of a single pentacene molecule was optimized by the B3LYP method with the 6-31G(*d*) basis set using GAUSSIAN03.⁴⁰ The molecule was treated as a rigid body throughout the subsequent calculations. We used the optimized geometry instead of the x-ray diffraction analysis data for the single pentacene molecule in order to avoid differences in the electronic structure imposed by the intramolecular interactions. This procedure allows a meaningful comparison of the electronic structures between the different polymorphs.

The lattice parameters obtained from x-ray diffraction of the single-crystal,²² bulk,⁴¹ and thin-film³⁷ phases are summarized in Table I. For the bulk phase, we adopted the recent powder diffraction analysis data⁴¹ rather than the data of Campbell *et al.*²⁷ because they show more precise agreement with the recent GIXD results.^{26,42} In addition, the a and b axes are interconverted and the c axis is taken as the 011 direction (the unit vectors of the lattice in the real space, $\mathbf{a}, \mathbf{b}, \mathbf{c}$, are converted to $\mathbf{b}, \mathbf{a}, \mathbf{b} + \mathbf{c}$) to facilitate a better comparison of the band structure with the other polymorphs.

The molecular orientations of the bulk and single-crystal phases were obtained from the single-crystal x-ray structural data.^{22,27} The molecular long and short axes were determined using the least-squares method. Those of the thin-film were

determined by comparing the calculated diffraction intensities with the reported x-ray reciprocal space map.³⁷ The crystal structures were constructed from the molecular orientations and the optimized molecular structure. They were further optimized using the Dreiding force field⁴³ on CERIU2 program (Accelrys) with fixed lattice parameters.⁴⁴ The obtained molecular orientations and structures are shown in Table I and Fig. 1, respectively. The molecular orientations are expressed in terms of the Euler angles, ω, χ, ϕ . The y axis is parallel to the b axis, and the x axis is in the ab plane while the z axis is parallel to the c^* axis. The atom positions in the crystal (x, y, z) are converted from the reference positions (x', y', z'),

$$\begin{pmatrix} x \\ y \\ z \end{pmatrix} = R_z(\phi)R_y(\chi)R_z(\omega) \begin{pmatrix} x' \\ y' \\ z' \end{pmatrix}, \quad (1)$$

where R_ν is a matrix that expresses the rotation around the ν axis. The z' and y' axes are parallel to the molecular long and short axes, respectively, and the x' axis is normal to the molecular plane.

In order to assess the reliability of the obtained geometry, the structure of the thin film was also optimized using COMPASS (condensed-phase optimized molecular potentials for atomistic simulation studies).⁴⁵ As shown in Table I, although the structure is slightly different, the difference in the calculated band energies was found to be less than 50 meV.

The energy bands were calculated using the CASTEP code⁴⁶ on MATERIAL STUDIO program (Accelrys). The generalized gradient approximation (GGA) of the Perdew-Burke-Ernzerhof functional (PBE) was applied for the exchange-correlation energy. The plane wave basis set cutoff was 310 eV and the ultrasoft pseudopotential was used. The \mathbf{k} point for Brillouin zone was sampled at $3 \times 4 \times 2$ mesh points.

III. EXPERIMENT

Pentacene was purchased from Tokyo Kasei Kogyo Co. Ltd. and purified by three cycles of vacuum sublimation.

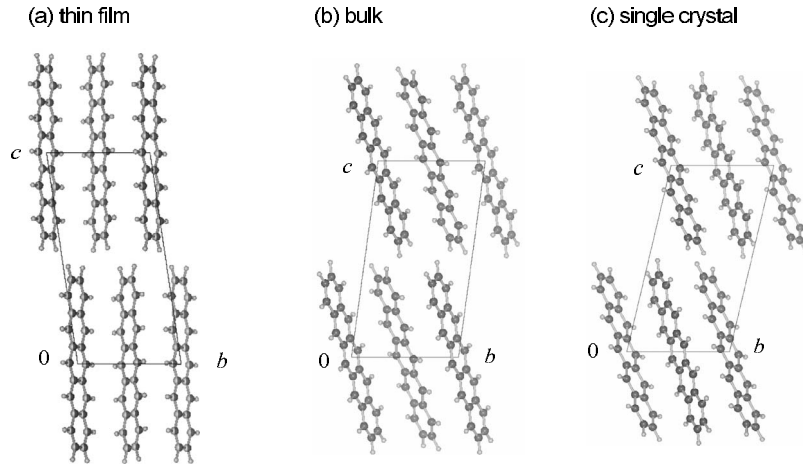


FIG. 1. The crystallographic structure of the pentacene (a) thin-film, (b) bulk, and (c) single-crystal phases.

Si(100) wafers were treated with buffered HF (HF:NH₄F = 1:10) to remove the thick insulating oxide layer and then irradiated by UV light in air for a few minutes to grow a thin oxide layer.

Pentacene was deposited at room temperature in a vacuum lower than 1×10^{-5} Pa. The thin-film phase was prepared as a 5-nm-thick film grown at a deposition rate of 0.01 nm s^{-1} and the bulk phase as a 230-nm-thick film grown at a deposition rate of 0.2 nm s^{-1} . In the previous work, we confirmed that the bulk phase grows on top of the thin-film phase.²⁶ We estimated that the top 100 nm layer of the present sample belongs to the bulk phase. The inelastic mean free path of an electron in most organic compounds is not larger than 1 nm (Refs. 47 and 48) in electron kinetic energy region of UPS. Thus, the photoemission spectra of the 230-nm-thick film originate almost completely from the bulk phase. Photoemission spectra were measured *in situ* using a SPECS Phoibos 150 analyzer with a He I discharge lamp ($h\nu=21.218 \text{ eV}$). The background pressure during the sample depositions and measurements was about 1×10^{-5} Pa.

The structures of the sample films were subsequently analyzed with x-ray diffraction (Rigaku, ATX-G) using a Cu $K\alpha$ ($\lambda=0.154184 \text{ nm}$) x-ray source. Polymorphs of the films were examined from 001 and $0\bar{2}1$ diffractions. The rocking scan of 001 diffractions showed that the c^* axes were normal to the substrate surface plane within the experimental uncertainty of about 0.1° in both the thin-film and bulk phases. The crystalline domains were randomly oriented around the c^* axis in both films as observed from the rocking scan of the $1\bar{1}0$ diffraction.

IV. RESULT AND DISCUSSION

A. Band structure

The energy bands calculated for the three polymorphs of pentacene are plotted in Figs. 2–4 where the symmetry points $\Gamma(0,0,0)$, $X(1/2,0,0)$, $Y(0,1/2,0)$, $Z(0,0,1/2)$, $M(1/2,1/2,0)$, and $M'(1/2,-1/2,0)$ are chosen in terms of the unit vectors of the lattice in reciprocal space.

The results for the single crystal and bulk phases qualitatively reproduce the previous reports.^{12–20} Each of HOMO-1, HOMO, lowest unoccupied molecular orbital (LUMO), and LUMO+1 levels forms two bands due to the two inequivalent pentacene molecules in the unit cell. The bandwidth of the Γ -Z direction is smaller due to the small overlap of the π orbitals along the molecular long axis. The largest energy dispersions were observed in the Γ -M and Γ -M' directions. The total widths of HOMO-derived bands are 487 and 365 meV, respectively, for the single-crystal and bulk phases.

The band structure for the thin-film phase is significantly different. The bandwidths are larger and isotropic in all the directions calculated except for the Γ -Z direction. The total bandwidth for the HOMO-derived band is 603 meV. The energy between the two subbands is the largest at the Γ point.

The band dispersion in pentacene was first experimentally observed by Koch *et al.*⁷ They applied angle- and energy-

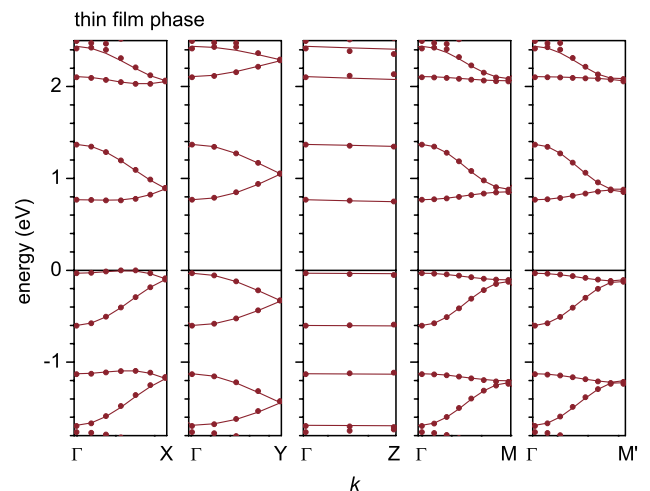


FIG. 2. (Color online) Energy bands of the pentacene thin-film phase obtained from the GGA-PBE calculation (dots) and the tight-binding fits (solid lines) for the HOMO-1, HOMO, LUMO, and LUMO+1.

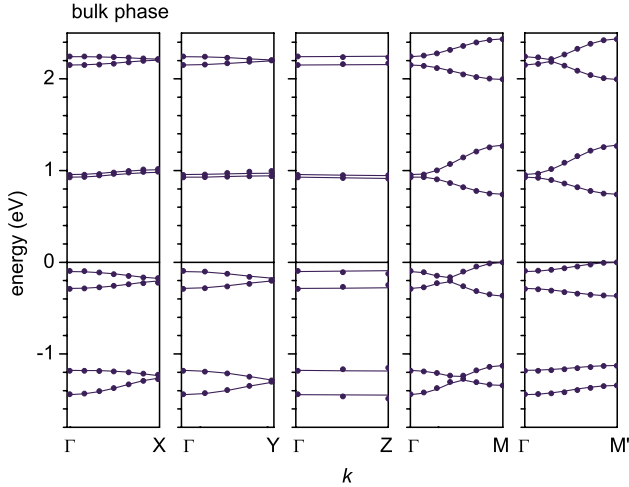


FIG. 3. (Color online) Energy bands of the pentacene bulk phase obtained from the GGA-PBE calculation (dots) and the tight-binding fits (solid lines) for the HOMO-1, HOMO, LUMO, and LUMO+1.

dependent UPS to a pentacene film deposited on highly oriented pyrolytic graphite (HOPG) and observed the energy dispersion along the surface normal direction. The measurement seems to be carried out along the b axis judging from the reported lattice spacing of about 0.74 nm (note $a < b$), though the structure of the film was not clear.

More precise band structures were reported on pentacene monolayer fabricated on Bi(001) surface using angle-resolved photoemission spectroscopy.⁸ The film structure was confirmed to be the bulk phase from reflection high-energy electron diffraction (RHEED). The maximum dispersions of the HOMO-derived bands observed along Γ - M or Γ - M' (M and M' were not distinguished experimentally) were reported to be about 400 meV. The bandwidth qualitatively agrees with our calculation for the bulk phase. An

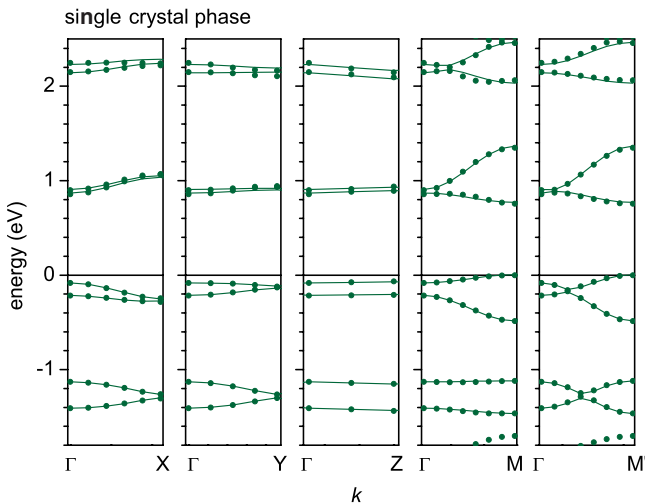


FIG. 4. (Color online) Energy bands of the pentacene single-crystal phase obtained from the GGA-PBE calculation (dots) and the tight-binding fit (solid lines) for the HOMO-1, HOMO, LUMO, and LUMO+1.

apparent difference may be the dispersion behavior as discussed in Ref. 8. The experimental bands show the smallest splitting at the Γ point where the calculation predicts a large splitting. It may be that the film structure was different from the bulk phase. Also, the influence of the electronic states of the substrate cannot be excluded because a pentacene monolayer was used for the measurement.

Note that the one-dimensional tight-binding model has been used to interpret the experimental energy dispersion in these works,^{7,8} though the one-dimensional model cannot reproduce the band dispersion of pentacene. As will be seen below, two-dimensional tight-binding approximation with at least three transfer integrals is required to appropriately describe the band structures of pentacene.

B. Comparison with the tight-binding model

Since the band structure of the pentacene crystal is well accounted for the tight-binding approximation,^{13,14,18} we will compare the energy bands calculated above with those derived from the tight-binding model to discuss intermolecular interactions of each pair of constituent molecules. In this model, the energy dispersions of the two bands, $E_+(\mathbf{k})$ and $E_-(\mathbf{k})$, with respect to the energy E_0 are expressed as

$$E_{\pm}(\mathbf{k}) = E_0 + T_1 \pm \left[T_2^2 + \left(\frac{\Delta E}{2} \right)^2 \right]^{1/2}, \quad (2)$$

where \mathbf{k} is the wave vector and ΔE accounts for the energy difference between the two inequivalent sites. T_1 and T_2 stand for interactions of the molecules between the equivalent and inequivalent sites, respectively, and are connected with transfer integrals t_i and t_j ,

$$T_1 = 2 \sum_i t_i \cos(\mathbf{k} \cdot \mathbf{r}_i),$$

$$T_2 = 2 \sum_j t_j \cos(\mathbf{k} \cdot \mathbf{r}_j), \quad (3)$$

where each sum is calculated over the molecules of translationally equivalent i and inequivalent j sites. In this work, 13 and 8 combinations of nearest neighbor molecules were chosen for T_1 and T_2 , respectively. Using the least-squares method, Eqs. (2) and (3) are fitted to the band energy from the present GGA-PBE calculations with the fitting parameters of t_i , t_j , ΔE , and E_0 , which are summarized in Table II. The tight-binding bands, shown by solid lines in Figs. 2-4, are found to precisely reproduce the band structure calculated by the GGA-PBE method (shown by dots). The obtained transfer integrals for HOMO and LUMO in the single-crystal phase agree well with the previously reported values,^{13,18} though the sign of t_{100} for HOMO is opposite to that reported in Ref. 14.

From Table II, only t_{100} , $t_{1/2 \ 1/2 \ 0}$, and $t_{1/2 \ 1/\sqrt{2} \ 0}$ have significant values while the other transfer integrals are negligible (less than 10 meV in absolute value). Actually, the two-dimensional band structures along the a^*b^* plane are reproduced by only the three transfer integrals t_{100} , $t_{1/2 \ 1/2 \ 0}$, and $t_{1/2 \ 1/\sqrt{2} \ 0}$ in addition to E_0 and ΔE . Although a similar

TABLE II. The parameters obtained by fitting the tight-binding approximation [Eqs. (2) and (3)] to the energy bands calculated by the GGA-PBE method.

				HOMO-1			HOMO			LUMO			LUMO+1		
				Thin film	Bulk	Single crystal	Thin film	Bulk	Single crystal	Thin film	Bulk	Single crystal	Thin film	Bulk	Single crystal
E_0 (meV)				-1303	-1276	-1289	-218	-189	-204	961	975	977	2187	2208	2200
ΔE (meV)				6	34	47	8	24	38	7	21	34	8	26	33
t_{hkl} (meV)				h	k	ℓ									
	1	0	0	-57	-18	3	-53	1	24	44	-13	-33	53	-3	-23
	0	1	0	8	-2	-2	4	-3	-1	5	-4	-6	-5	-1	0
	2	0	0	0	0	-1	-1	-1	-1	0	0	0	-3	1	0
	0	2	0	0	0	0	0	0	0	0	0	0	-1	0	-1
	1	1	0	-3	-3	2	0	0	2	-1	-1	-2	-3	1	-1
	1	-1	0	-3	3	-3	-1	3	0	-1	-2	-1	-3	-1	0
	0	0	1	-2	1	0	2	-1	2	5	1	-2	-4	-1	0
	0	1	1	0	0	0	0	0	0	0	0	0	0	0	0
	0	1	-1	0	-2	4	0	2	-4	0	0	1	1	0	2
	1	0	1	0	0	0	-1	0	0	0	0	0	1	0	1
	1	0	-1	0	2	-1	0	-1	2	0	0	-2	1	0	4
	1	1	-1	0	0	0	0	0	0	0	0	0	1	0	0
	1	1	-1	0	0	1	0	0	-2	0	0	-6	0	0	13
	1/2	1/2	0	68	66	-7	68	-63	-43	73	-69	-82	39	-42	-65
	1/2	-1/2	0	72	6	80	73	24	79	80	70	83	46	61	51
	1/2	1/2	-1	-1	-8	1	0	-7	-1	0	-1	9	2	-2	-6
	1/2	-1/2	1	0	-2	-1	0	-2	-1	0	-4	-1	2	6	-2
	3/2	3/2	0	0	0	0	0	0	-1	0	0	0	-2	0	0
	3/2	-3/2	0	0	0	0	0	0	1	0	0	0	-2	0	-1
	3/2	1/2	0	1	2	-1	0	-1	0	-2	-1	-1	-2	-1	-3
	3/2	-1/2	0	1	-1	1	-1	0	1	-1	2	2	-2	0	2

discussion was presented previously for band dispersion of the HOMO-derived bands, only the crystal structure of the single-crystal phase is correct among the four polymorphs examined.¹⁸

In the bulk and single-crystal phases, absolute values of $t_{1/2\ 1/2\ 0}$ and $t_{1/2\ \overline{1}\overline{2}\ 0}$ are about 40–80 meV. The signs of $t_{1/2\ 1/2\ 0}$ and $t_{1/2\ \overline{1}\overline{2}\ 0}$ are opposite causing destructive interference of $t_{1/2\ 1/2\ 0} \cos(\mathbf{k} \cdot (\mathbf{a} + \mathbf{b})/2)$ and $t_{1/2\ \overline{1}\overline{2}\ 0} \cos(\mathbf{k} \cdot (\mathbf{a} - \mathbf{b})/2)$ along the a^* and b^* in Eq. (3). This explains the large anisotropy of the energy dispersion: Small energy dispersions occur along Γ - X and Γ - Y , while the dispersions are large along Γ - M and Γ - M' .¹³ In the thin-film phase, $t_{1/2\ 1/2\ 0}$ and $t_{1/2\ \overline{1}\overline{2}\ 0}$ are about 70 meV, slightly larger than those in the bulk and single-crystal phases. The signs of $t_{1/2\ 1/2\ 0}$ and $t_{1/2\ \overline{1}\overline{2}\ 0}$ are always the same in the thin-film phase, which leads to isotropic energy dispersions within the a^*b^* plane (along Γ - X , Γ - Y , Γ - M , and Γ - M' in Fig. 2) due to the constructive interference of $t_{1/2\ 1/2\ 0} \cos(\mathbf{k} \cdot (\mathbf{a} + \mathbf{b})/2)$ and $t_{1/2\ \overline{1}\overline{2}\ 0} \cos(\mathbf{k} \cdot (\mathbf{a} - \mathbf{b})/2)$.

In contrast, the magnitude and the sign of t_{100} vary depending on the polymorphs and molecular orbitals. For example, t_{100} of HOMO is -50 meV in the thin-film phase, while $t_{100} = +29$ meV in the single-crystal phase is large but

opposite in sign. In the bulk phase, t_{100} is negligibly small (-1 meV). This behavior can be explained by the overlap between the molecular orbitals of the molecules located at (000) and (100). As shown in Fig. 5, the thin-film phase shows efficient overlap of the HOMO. In the bulk phase, the molecule is displaced along the long molecular axis; this displacement is about half of the distance between the nodal planes, resulting in a destructive overlap of the molecular orbitals and small t_{100} . The displacement along the long molecular axis in the single crystal is larger than that in the bulk phase. This makes for efficient overlap of the molecular orbitals again, although the sign of t_{100} is opposite to that of the thin-film phase.

In examining the sign of t_{100} among the different molecular orbitals, those shapes should also be considered. A nodal plane parallel to the molecular long axis and also normal to the molecular short axis exists in HOMO-1 and HOMO but not in LUMO and LUMO+1 as shown in Fig. 6. This nodal plane affects the sign of t_{100} ; the sign changes between HOMO and LUMO when viewed from HOMO-1 to LUMO+1 in each of the thin-film and single-crystal phases (in the bulk phase, the change is not clear as t_{100} is small).

Due to this nodal plane, the HOMO- and LUMO-derived bands look like mirror images with respect to the Fermi level

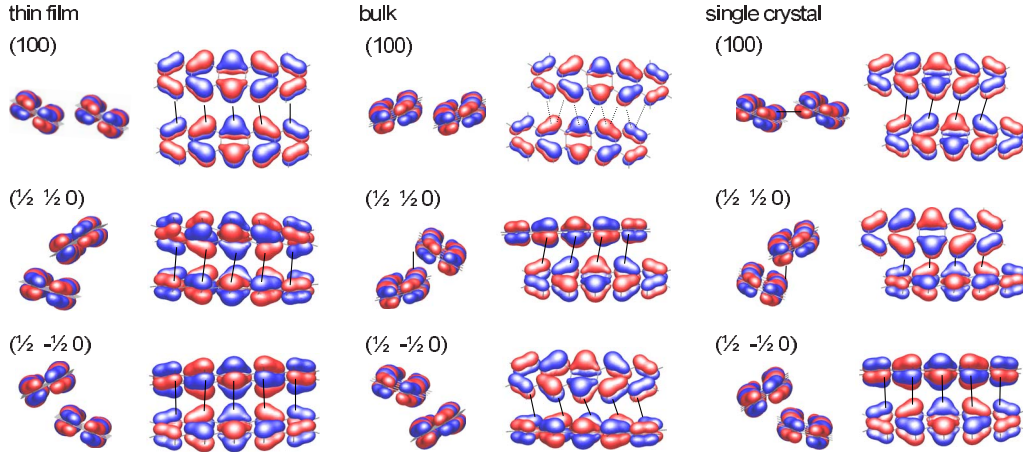


FIG. 5. (Color online) HOMO orbital overlap between two pentacene molecules at the (000) position with those at (1 0 0), (1/2 1/2 0), and (1/2 -1/2 0) for the three polymorphs.

(assumed at the middle of the band gap) in the thin-film and single-crystal phases. As seen from Eqs. (2) and (3), t_{100} governs the overall dispersion of the two subbands (i.e., average of the upper and lower bands), while $t_{1/2\ 1/2\ 0}$ and $t_{1/2\ \overline{1/2}\ 0}$ determine the energy difference between the upper and lower bands. This symmetric band structure is imposed by the sign of t_{100} , which is opposite between the HOMO- and LUMO-derived bands.

C. Band structures and polymorphs

We examine the three transfer integrals responsible for the band dispersions t_{100} , $t_{1/2\ 1/2\ 0}$, and $t_{1/2\ \overline{1/2}\ 0}$ to interpret the relation between the band structures and the crystallographic structures. Figure 5 shows the HOMO interactions between a central molecule and the nearest neighbor molecules located at (100), 1/2 1/2 0, and 1/2 1/2 0. These molecular overlaps are relevant to the sign and magnitude of the transfer integrals.

The pentacene molecules crystallize into the herringbone structure where the molecular long axes are almost parallel to each other and the angle between the molecular planes of the inequivalent molecules always falls in the range between 50° and 53° . Mattheus *et al.*²⁸ noted that the structure projected along the long molecular axis is preserved over the different polymorphs of pentacene. Hence, the structures of pentacene shown in Fig. 1 are characterized only by the angle between the molecular long axis and the c^* axis. This orientation angle of the molecules imposes the displacement along the molecular long axes λ_{hkl} as shown in Fig. 7. In this figure, the λ_{hkl} values are also shown where the molecular long axis is defined by the sum of the two vectors that signify molecular long axes of two independent pentacene molecules. Due to the inversion symmetry of the pentacene crystals, relations of $\lambda_{1/2\ 1/2\ 0} = (\lambda_{100} + \lambda_{010})/2$ and so on should hold. λ_{hkl} for any (hkl) is close to zero in the thin-film phase as a result of small angle between the molecular long axis and the c^* axis. In the bulk and single-crystal phases, $\lambda_{1/2\ 1/2\ 0}$ and λ_{100} is large while $\lambda_{1/2\ \overline{1/2}\ 0}$ is always small.

We extend this model to analyze the magnitude and sign of t_{hkl} . For this purpose, we must first discuss the overlaps of the molecular orbitals and λ_{hkl} . The displacement λ_{hkl} should be compared with a unit length that characterizes the shape of the molecular orbital along the molecular long axis; as the unit length, we use an average length d between the nodal planes of the molecular orbital along the molecular long axis as schematically illustrated in Fig. 6 where we assume $d = 1.6\text{ nm}/(n+1)$ from the pentacene molecular length, 1.6 nm. The number of nodal planes along the long molecular axis n is 3, 4, 6, and 7 for HOMO-1, HOMO, LUMO, and LUMO+1, respectively, as seen from Fig. 6.

The overlap of the molecular orbitals and t_{hkl} are classified by λ_{hkl}/d as follows: (i) When $\lambda_{hkl}/d = 0, \pm 2, \dots$, the

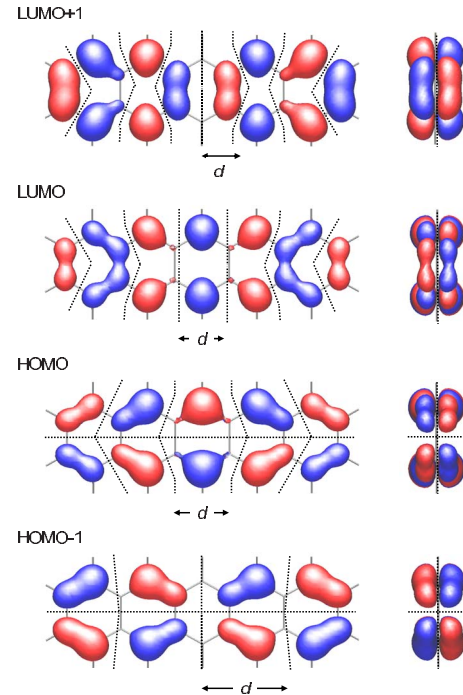


FIG. 6. (Color online) Molecular frontier orbitals of pentacene. The dotted lines show nodal planes.

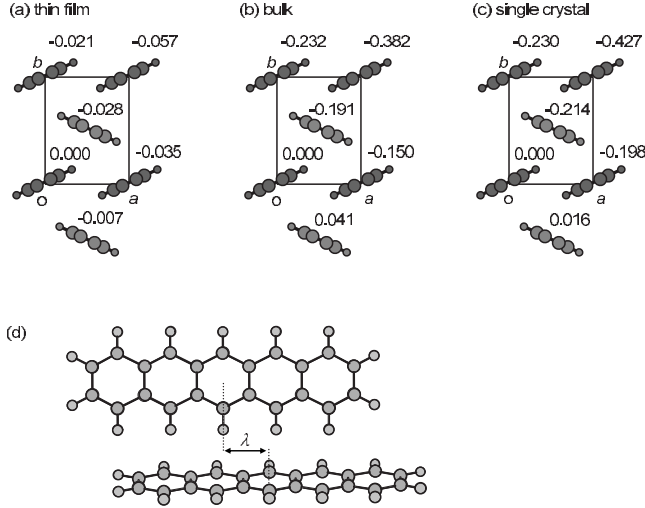


FIG. 7. Projections along the long molecular axes of the pentacene crystallographic structures for the (a) thin-film, (b) bulk, and (c) single-crystal phases. Definition of the displacement of the molecules along the molecular long axes λ_{hkl} is given in panel (d). The numbers of molecules at (h, k, ℓ) in panels (a), (b), and (c) designate λ_{hkl} in nm with respect to the $(0, 0, 0)$ molecules.

overlap of the molecular orbitals is efficient and t_{hkl} is large. (ii) When $\lambda_{hkl}/d = \pm 0.5, \pm 1.5, \pm 2.5, \dots$, the overlap of the molecular orbitals is canceled out and t_{hkl} is almost zero. (iii) When $\lambda_{hkl}/d = \pm 1, \pm 3, \dots$, the overlap of the molecular orbitals is again efficient, and t_{hkl} is large but the sign is opposite to case (i). In this way, the magnitude and sign of the transfer integrals can be predicted from the magnitude of λ_{hkl}/d . Figure 8 shows t'_{hkl} as a function of the ratio λ_{hkl}/d for the HOMO-1, HOMO, LUMO, and LUMO+1 in the three polymorphs. The transfer integral t'_{hkl} has the same magnitude with t_{hkl} , but the sign is opposite in $t_{1/2 1/2 0}$,

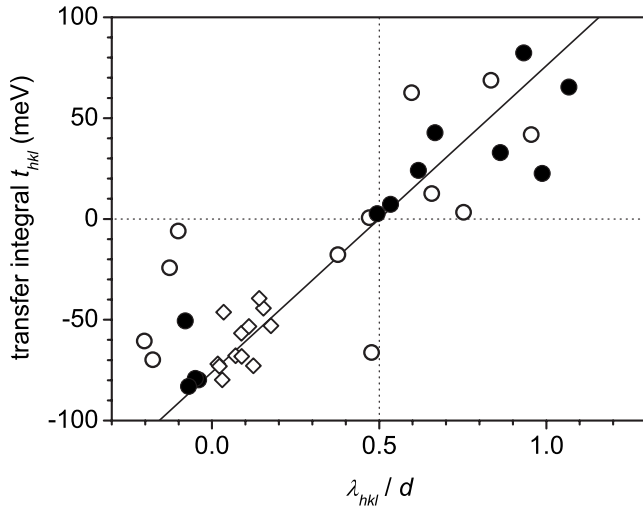


FIG. 8. Correlation between transfer integrals t'_{hkl} and λ_{hkl}/d for the pentacene thin-film (\diamond), bulk (\circ), and single-crystal (\bullet) phases. λ_{hkl}/d is a measure of the orbital overlap of the nearest neighbor molecules with $hkl=(001), (1/2 1/2 0), (1/2 -1/2 0)$. Definitions of λ_{hkl} and d are given in Figs. 6 and 7, respectively. A linear regression of the data is indicated by the solid line.

$t_{1/2 \bar{1}\bar{2} 0}$ for all the orbitals and t_{100} for LUMO and LUMO+1 to take into the above consideration the sign of t_{hkl} and the nodal plane of the molecular orbital. The correlation is fairly good.

According to this discussion, we can understand the correlation between the energy dispersion and the polymorphs. As mentioned above, anisotropy of the band structure in the a^*b^* plane is governed by the signs of $t_{1/2 1/2 0}$ and $t_{1/2 \bar{1}\bar{2} 0}$. In the bulk and single-crystal phases, the pentacene molecules are tilted by about 20° from the c^* axis and the displacement $\lambda_{1/2 \bar{1}\bar{2} 0}$ is large. These large angles cause $\lambda_{1/2 1/2 0}/d \approx 0$ and $\lambda_{1/2 \bar{1}\bar{2} 0}/d \approx -1$. As a result, $t_{1/2 1/2 0}$ and $t_{1/2 \bar{1}\bar{2} 0}$ have the opposite signs, leading to the anisotropic band structures. On the other hand, the molecules are almost parallel to the c^* axis and $\lambda_{1/2 1/2 0}/d \approx 0$ and $\lambda_{1/2 \bar{1}\bar{2} 0}/d \approx 0$ in the thin-film phase. This explains the isotropic band structure.

D. Effective masses of the charge carriers

The transport properties of charge carriers in semiconductors are in the framework of band theory characterized by the effective mass near the band edge. The effective masses m^* and the components of the reciprocal effective mass tensors $(1/m^*)_{\mu\nu}$ are calculated from the relation

$$\left(\frac{1}{m^*}\right)_{\mu\nu} = \frac{1}{\hbar^2} \frac{d^2 E(\mathbf{k})}{d\mu d\nu}, \quad (4)$$

where $E(\mathbf{k})$ is given by Eq. (2). μ and ν are Cartesian coordinates given in Sec. II. The results are summarized in Table III. Negative values of m^* signify the effective mass of the hole. m^* and $(1/m^*)_{\mu\nu}$ are in good agreement with the values previously calculated for the bulk and single-crystal phases.^{13,17-19}

Although pentacene shows hole conductivity in many cases, the ambipolar field-effect mobility was recently reported in the pentacene field-effect transistor.⁴⁹ We therefore discuss the effective masses of both the holes located at the top of the HOMO-derived (valence) bands and the electrons at the bottom of the LUMO-derived (conduction) bands.

The effective mass of the hole in the thin-film phase is almost isotropic and ranges from $-2m_0$ to $-3m_0$ along the ab plane. The effective mass of the single-crystal phase is largely anisotropic and its magnitude is only small along the b direction as reported previously.¹³ The effective masses and their reciprocal tensors of the LUMO-derived bands are similar to those of the HOMO-derived bands for each polymorph except that the signs are opposite. The minimum of the effective mass falls in the range from $2m_0$ to $3m_0$. As a whole, the properties of the electrons and the holes predicted from the constant energy surfaces and the effective masses appear to be significantly similar. These results suggest that the holes and the electrons behave in a same way in each of the three polymorphs of pentacene as far as the band transport is concerned. The same discussion can be done from the isoenergy surfaces near the band edges of HOMO and LUMO.⁵⁰

TABLE III. The effective masses m^* for holes and electrons calculated, respectively, from the HOMO- and LUMO-derived bands of the three polymorphs of pentacene. The reciprocal effective mass tensors $(1/m^*)_{\mu\nu}$ and the averages of three principal components m^* are shown. The x , y , and z axes are as defined in the text.

		HOMO			LUMO		
		Thin film	Bulk	Single crystal	Thin film	Bulk	Single crystal
$m_0(1/m^*)_{\mu\nu}$	xx	-0.33	-0.20	-0.05	0.17	0.21	0.04
	yy	-0.42	-0.44	-0.53	0.44	0.54	0.51
	zz	-0.16	-0.22	-0.12	0.34	0.22	0.18
	xy	0.02	-0.08	0.08	-0.02	-0.02	-0.05
	yz	0.00	-0.02	0.01	-0.06	-0.02	0.08
	zx	0.02	0.08	-0.04	-0.02	0.11	-0.01
m^*/m_0	Average	-3.31	-3.48	-4.33	3.16	3.09	4.13

Note that the charge carrier properties discussed here do not directly correspond to the bandwidths which are frequently used as a measure of the carrier mobility. This is because the effective mass is characterized only by the local structure of the band near the band edge. For example, the effective mass is heavier (i.e., less mobile as a charge carrier) in the thin-film phase than in the other phases, though the bandwidth is larger. The bandwidth and the effective mass predict opposite results in preferable direction of the carrier mobility; the lightest effective mass is obtained near the b^* direction in the single-crystal phase, although as shown in Fig. 4, only a small energy dispersion is found in this direction.

E. Calculated density of states and photoemission spectra

In this section, the calculated DOS is compared with the UPS spectra. The DOS is calculated by numerically integrating the tight-binding bands $E_{\pm}(\mathbf{k})$ [given by Eq. (2)] over \mathbf{k} . The obtained DOSs were subsequently convoluted with a Gaussian function having a full width at half maximum (FWHM) of 0.2 eV to facilitate the comparison with the experimental spectra. Figure 9 shows DOS for the energy region corresponding to the HOMO for the three polymorphs. The thin-film phase shows an asymmetric DOS which exhibits a peak at -0.13 eV and tailing to -0.5 eV because of the large and isotropic band dispersion. The bulk phase shows a single symmetric feature due to the small energy dispersion. In the single-crystal phase, the energy dispersion is large along the Γ - M and Γ - M' directions. However, the small dispersion along the Γ - X , Γ - Y , and Γ - Z directions produces a dense DOS in the range from -0.1 to -0.2 eV. The resultant feature will be a single symmetric peak.

The experimental spectra of the HOMO region are shown in Fig. 10. The spectral features are in good agreement with the calculated DOS in Fig. 9. The line shape is asymmetric in the thin-film phase, while in the bulk phase, a symmetric Gaussian shape is observed. The peak width is larger in the thin-film phase than that of the bulk phase. Although UPS of

the single crystal phase has not been reported yet, a symmetric Gaussian shape is expected.

The spectral line shape of the thin-film phase is similar to those reported of pentacene films on SiO_2 (Refs. 7 and 39) and on a copper phthalocyanine layer.³⁹ The authors of Refs. 7 and 39 suggest the asymmetric line shape of HOMO-derived feature is caused by band dispersion of the pentacene

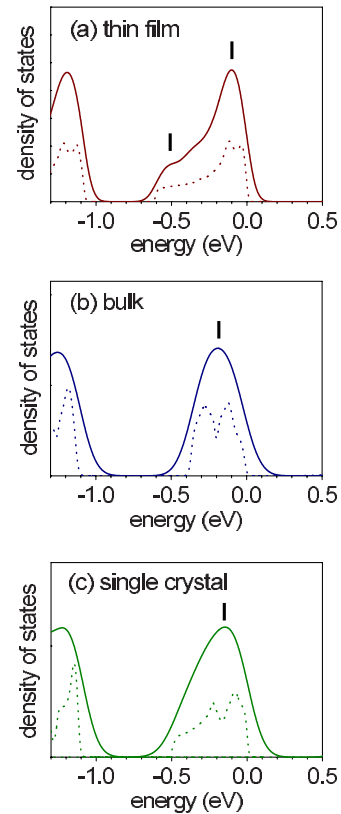


FIG. 9. (Color online) Calculated density of states (DOS) for the pentacene (a) thin-film, (b) bulk, and (c) single-crystal (c) phases. The calculated points (dotted lines) are convoluted with a Gaussian function of 0.2 eV FWHM (solid lines).

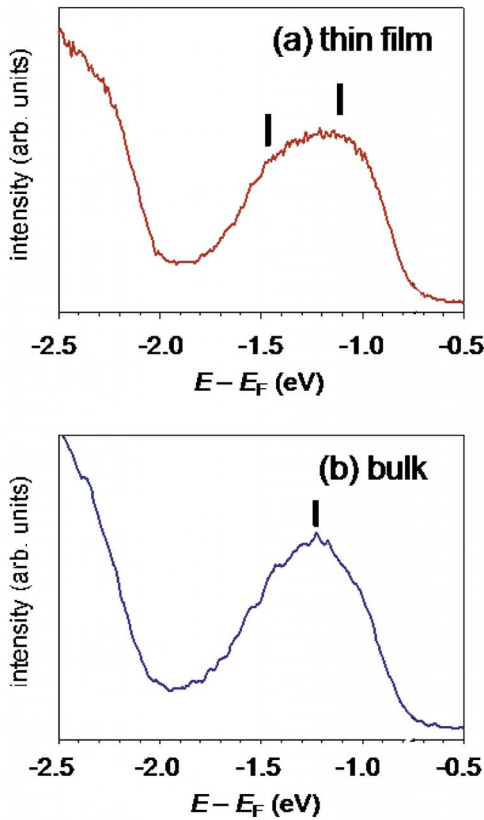


FIG. 10. (Color online) Angle-integrated photoemission spectra of the HOMO region in the pentacene (a) thin-film and (b) bulk phases.

crystal. This line shape is not found in the pentacene films prepared on HOPG. They mentioned that the energy dispersions arise from the “standing” orientation of the pentacene molecules, as this is required in the wave vector conservation in the photoemission process. Our results confirm that the origin of the asymmetric line shape is band dispersion. However, the molecular orientation is not an only requirement as the polymorph is also an important factor.

V. CONCLUSION

In this work, the energy bands of pentacene in the thin-film, bulk, and single-crystal phases have been calculated using the GGA-PBE method with the plane wave basis functions. For the structure of the thin-film phase, we used the recent crystallographic data derived from our x-ray reciprocal space map which is likely the most reliable at the moment.

The calculated energy band structures are essentially two dimensional, that is, little dispersion is noticed along the c^* direction. The energy dispersions of the bulk and single-crystal phases are largely anisotropic while the bandwidth is larger in the single-crystal phase. In contrast, the band structure of the thin-film phase is remarkably isotropic and shows larger bandwidth than the other phases.

The band dispersions were compared with those based on the tight-binding approximation to evaluate transfer inte-

grals. The dispersions of the bands derived from HOMO-1, HOMO, LUMO, and LUMO+1 are well described by the three-dimensional tight-binding bands. Only a few transfer integrals of nearest neighbor interactions play an important role, in particular, three transfer integrals t_{100} , $t_{1/2\ 1/2\ 0}$, and $t_{1/2\ \overline{1}\overline{1}\ 0}$ accounting for the intermolecular interactions of the molecules along the a , $(a+b)/2$, and $(a-b)/2$ directions. The anisotropic energy dispersion of the bulk and single-crystal phases is explained by the opposite signs of $t_{1/2\ 1/2\ 0}$ and $t_{1/2\ \overline{1}\overline{1}\ 0}$, while the source of the large and isotropic band dispersion of the thin-film phase is of the same sign as $t_{1/2\ 1/2\ 0}$ and $t_{1/2\ \overline{1}\overline{1}\ 0}$. The signs of t_{100} between HOMO- and LUMO-derived bands are opposite in both the thin-film and single-crystal phases. In the bulk phase, on the other hand, the magnitude of t_{100} is small. As a result, the band structure is symmetric with respect to the Fermi level between the HOMO- and LUMO-derived bands.

The magnitudes and signs of the transfer integrals t_{100} , $t_{1/2\ 1/2\ 0}$, and $t_{1/2\ \overline{1}\overline{1}\ 0}$ are understood in terms of the displacement of molecules along the molecular long axes $\lambda_{hk\ell}$ and the shape of the molecular orbitals. A parameter $\lambda_{hk\ell}/d$ was introduced to describe variations in overlaps of the molecular orbitals. Since $\lambda_{hk\ell}$ originates from the angles between the molecular long axes and the c^* axis, the similar energy dispersions observed for the bulk and single-crystal phases are likely a result of the large angles, while the band dispersion of the thin-film phase is characterized by the small angle.

As the properties of the charge carriers near the band edges are relevant to the transport properties, the effective masses for HOMO- and LUMO-derived bands are discussed. The effective mass for the thin-film phase is isotropic in the ab plane, while anisotropic in the single-crystal phase and moderately anisotropic in the bulk phase. The minimum of the absolute value of the effective mass is about $2m_0-3m_0$ for all phases. The effective masses for the hole and electron are quite similar. These similarities suggest that the electron and the hole behave in a similar way in pentacene if the band transport is established.

Finally, we calculated the density of states to interpret the spectral line shapes of the HOMO region measured by angle-integrated photoemission spectroscopy of the thin-film and bulk phases. The calculated DOS and the experimental spectra are in good agreement. The HOMO-derived band of the thin-film phase is asymmetric, which results from the large and isotropic energy dispersion. On the other hand, the bulk phase shows a symmetric Gaussian line shape due to the small energy dispersion of this phase.

ACKNOWLEDGMENTS

We would like to thank Y. Morikawa of Osaka University for helpful instruction on the band calculation. The calculations were carried out at the Supercomputer Laboratory, Institute for Chemical Research, Kyoto University. We acknowledge T. Terashima and M. Takano of Kyoto University for allowing us to use the x-ray diffractometer. This work was supported by a Grant-in-Aid for Scientific Research on Priority Areas of Molecular Conductors No. 15073214 from the Ministry of Education, Culture, Sports, Science, and Technology of Japan.

*FAX: +81-774-38-3084; yoshida@e.kuicr.kyoto-u.ac.jp

- ¹K. Seki, Y. Harada, K. Ohno, and H. Inokuchi, *Bull. Chem. Soc. Jpn.* **47**, 1608 (1974).
- ²S. Hasegawa, T. Mori, K. Imaeda, S. Tanaka, Y. Yamashita, H. Inokuchi, H. Fujimoto, K. Seki, and N. Ueno, *J. Chem. Phys.* **100**, 6969 (1994).
- ³N. Ueno, A. Kitamura, K. K. Okudaira, T. Miyamae, Y. Harada, S. Hasegawa, H. Ishii, H. Inokuchi, T. Fujikawa, T. Miyazaki, and K. Seki, *J. Chem. Phys.* **107**, 2079 (1997).
- ⁴Y. Azuma, T. Hasebe, T. Miyamae, K. K. Okudaira, Y. Harada, K. Seki, E. Morikawa, V. Saile, and N. Ueno, *J. Synchrotron Radiat.* **5**, 1044 (1998).
- ⁵H. Yamane, S. Kera, K. K. Okudaira, D. Yoshimura, K. Seki, and N. Ueno, *Phys. Rev. B* **68**, 033102 (2003).
- ⁶X. Crispin, J. Cornil, R. Friedlein, K. K. Okudaira, V. Lemaire, A. Crispin, G. Kestemont, M. Lehmann, M. Fahlman, R. Lazarzani, Y. Geerts, G. Wendin, N. Ueno, J.-L. Bredas, and W. R. Salaneck, *J. Am. Chem. Soc.* **126**, 11889 (2004).
- ⁷N. Koch, A. Vollmer, I. Salzmann, B. Nickel, H. Weiss, and J. P. Rabe, *Phys. Rev. Lett.* **96**, 156803 (2006).
- ⁸H. Kakuta, T. Hirahara, I. Matsuda, T. Nagao, S. Hasegawa, N. Ueno, and K. Sakamoto, *Phys. Rev. Lett.* **98**, 247601 (2007).
- ⁹T. Suzuki, T. Shimada, K. Ueno, S. Ikeda, K. Saiki, and T. Hasegawa, in *Organic Electronics: Materials, Devices, and Applications*, edited by F. So, G. B. Blanchet, and Y. Ohmon, MRS Symposia Proceedings No. 965E (Materials Research Society, Pittsburgh, 2006), p. 0965-S06-19.
- ¹⁰N. Karl, *Synth. Met.* **133**, 649 (2003).
- ¹¹O. D. Jurchescu, J. Baas, and T. T. M. Palstra, *Appl. Phys. Lett.* **84**, 3061 (2004).
- ¹²R. C. Haddon, X. Chi, M. E. Itkis, J. E. Anthony, D. L. Eaton, T. Siegrist, C. C. Mattheus, and T. T. M. Palstra, *J. Phys. Chem. B* **106**, 8288 (2002).
- ¹³G. A. de Wijs, C. C. Mattheus, R. A. de Groot, and T. T. M. Palstra, *Synth. Met.* **139**, 109 (2003).
- ¹⁴Y. C. Cheng, R. J. Silbey, D. A. da Silva, J. P. Calbert, J. Cornil, and J. L. Bredas, *J. Chem. Phys.* **118**, 3764 (2003).
- ¹⁵M. L. Tiago, J. E. Northrup, and S. G. Louie, *Phys. Rev. B* **67**, 115212 (2003).
- ¹⁶R. G. Endres, C. Y. Fong, L. H. Yang, G. Witte, and C. Woll, *Comput. Mater. Sci.* **29**, 362 (2004).
- ¹⁷K. Hummer and C. Ambrosch-Draxl, *Phys. Rev. B* **72**, 205205 (2005).
- ¹⁸A. Troisi and G. Orlandi, *J. Phys. Chem. B* **109**, 1849 (2005).
- ¹⁹K. Doi, K. Yoshida, H. Nakano, A. Tachibana, T. Tanabe, Y. Kojima, and K. Okazaki, *J. Appl. Phys.* **98**, 113709 (2005).
- ²⁰P. Parisse, L. Ottaviano, B. Delley, and S. Picozzi, *J. Phys.: Condens. Matter* **19**, 106209 (2007).
- ²¹D. Holmes, S. Kumaraswamy, A. J. Matzger, and K. P. C. Vollhardt, *Chem.-Eur. J.* **5**, 3399 (1999).
- ²²C. C. Mattheus, A. B. Dros, J. Baas, A. Meetsma, J. L. de Boer, and T. T. M. Palstra, *Acta Crystallogr., Sect. C: Cryst. Struct. Commun.* **57**, 939 (2001).
- ²³C. D. Dimitrakopoulos, A. R. Brown, and A. Pomp, *J. Appl. Phys.* **80**, 2501 (1996).
- ²⁴I. P. M. Bouchoms, W. A. Schoonveld, J. Vrijmoeth, and T. M. Klapwijk, *Synth. Met.* **104**, 175 (1999).
- ²⁵D. J. Gundlach, T. N. Jackson, D. G. Schlom, and S. F. Nelson, *Appl. Phys. Lett.* **74**, 3302 (1999).
- ²⁶H. Yoshida and N. Sato, *Appl. Phys. Lett.* **89**, 101919 (2006).
- ²⁷R. B. Campbell, J. Trotter, and J. Monteath, *Acta Crystallogr.* **15**, 289 (1962).
- ²⁸C. C. Mattheus, A. B. Dros, J. Baas, G. T. Oostergetel, A. Meetsma, J. L. de Boer, and T. T. M. Palstra, *Synth. Met.* **138**, 475 (2003).
- ²⁹T. Minakata, H. Imai, M. Ozaki, and K. Saco, *J. Appl. Phys.* **72**, 5220 (1992).
- ³⁰J. S. Wu and J. C. H. Spence, *J. Appl. Crystallogr.* **37**, 78 (2004).
- ³¹L. F. Drummy and D. C. Martin, *Adv. Mater. (Weinheim, Ger.)* **17**, 903 (2005).
- ³²T. Kiyomura, T. Nemoto, T. Ogawa, T. Minari, K. Yoshida, H. Kurata, and S. Isoda, *Jpn. J. Appl. Phys., Part 1* **45**, 401 (2006).
- ³³S. E. Fritz, S. M. Martin, C. D. Frisbie, M. D. Ward, and M. F. Toney, *J. Am. Chem. Soc.* **126**, 4084 (2004).
- ³⁴R. Ruiz, A. C. Mayer, G. G. Malliaras, B. Nickel, G. Scoles, A. Kazimirov, H. Kim, R. L. Headrick, and Z. Islam, *Appl. Phys. Lett.* **85**, 4926 (2004).
- ³⁵H. C. Yang, T. J. Shin, M. M. Ling, K. Cho, C. Y. Ryu, and Z. N. Bao, *J. Am. Chem. Soc.* **127**, 11542 (2005).
- ³⁶R. G. Della Valle, E. Venuti, A. Brillante, and A. Girlando, *J. Chem. Phys.* **118**, 807 (2003).
- ³⁷H. Yoshida, K. Inaba, and N. Sato, *Appl. Phys. Lett.* **90**, 181930 (2007).
- ³⁸N. Sato, K. Seki, H. Inokuchi, and Y. Harada, *Chem. Phys.* **109**, 157 (1986).
- ³⁹H. Fukagawa, H. Yamane, T. Kataoka, S. Kera, M. Nakamura, K. Kudo, and N. Ueno, *Phys. Rev. B* **73**, 245310 (2006).
- ⁴⁰M. J. Frisch, G. W. Trucks, H. B. Schlegel, G. E. Scuseria, M. A. Robb, J. R. Cheeseman, J. A. Montgomery, Jr., T. Vreven, T. Kudin, J. C. Burant, J. M. Millam, S. S. Iyengar, J. Tomasi, V. Barone, B. Mennucci, M. Cossi, G. Scalmani, N. Rega, G. A. Petersson, H. Nakatsuji, M. Hada, M. Ehara, K. Toyota, R. Fukuda, J. Hasegawa, M. Ishida, T. Nakajima, Y. Honda, O. Kitao, H. Nakai, M. Klene, X. Li, J. E. Knox, H. P. Hratchian, J. B. Cross, C. Adamo, J. Jaramillo, R. Gomperts, R. E. Stratmann, O. Yazyev, A. J. Austin, R. Cammi, C. Pomelli, J. W. Ochterski, P. Y. Ayala, K. Morokuma, G. A. Voth, P. Salvador, J. J. Dannenberg, V. G. Zakrzewski, S. Dapprich, A. D. Daniels, M. C. Strain, O. Farkas, D. K. Malick, A. D. Rabuck, K. Raghavachari, J. B. Foresman, J. V. Ortiz, Q. Cui, A. G. Baboul, S. Clifford, J. Cioslowski, B. B. Stefanov, G. Liu, A. Liashenko, P. Piskorz, I. Komaromi, R. L. Martin, D. J. Fox, T. Keith, M. A. Al-Laham, C. Y. Peng, A. Nanayakkara, M. Challacombe, P. M. W. Gill, B. Johnson, W. Chen, M. W. Wong, C. Gonzalez, and J. A. Pople, *GAUSSIAN 03, Revision B. 03*, Gaussian Inc., Pittsburgh, PA, 2003.
- ⁴¹L. Farina, A. Brillante, R. G. Della Valle, E. Venuti, M. Amboage, and K. Syassen, *Chem. Phys. Lett.* **375**, 490 (2003).
- ⁴²T. Kakudate, N. Yoshimoto, and Y. Saito, *Appl. Phys. Lett.* **90**, 081903 (2007).
- ⁴³S. L. Mayo, B. D. Olafson, and W. A. Goddard, *J. Phys. Chem.* **94**, 8897 (1990).
- ⁴⁴See EPAPS Document No. E-PRBMD0-77-038811 for the crystallographic structure of the thin-film phase (CIF file). For more information on EPAPS, see <http://www.aip.org/pubservs/epaps.html/>.
- ⁴⁵H. Sun, *J. Phys. Chem. B* **102**, 7338 (1998).
- ⁴⁶M. D. Segall, P. J. D. Lindan, M. J. Probert, C. J. Pickard, P. J. Hasnip, S. J. Clark, and M. C. Payne, *J. Phys. Condens. Matter* **14**, 2717 (2002).

⁴⁷M. P. Seah and W. A. Dench, *Surf. Interface Anal.* **1**, 2 (1979).

⁴⁸S. Tanuma, C. J. Powell, and D. R. Penn, *Surf. Interface Anal.* **21**, 165 (1993).

⁴⁹T. Yasuda, T. Goto, K. Fujita, and T. Tsutsui, *Appl. Phys. Lett.* **85**, 2098 (2004).

⁵⁰See EPAPS Document No. E-PRBMDO-77-038811 for the constant energy surfaces 5 meV below the band edge of the HOMO-derived band and that 5 meV above the LUMO-derived band. For more information on EPAPS, see <http://www.aip.org/pubservs/epaps.html/>.